

# AN *ASCA* STUDY OF THE W51 COMPLEX

Bon-Chul Koo and Jae-Joon Lee

*Astronomy Program, SEES, Seoul National University, Seoul 151-742, Korea;  
koo@astrohi.snu.ac.kr*

and

Frederick D. Seward

*Harvard-Smithsonian Center for Astrophysics, 60 Garden Street, Cambridge, MA 02138*

## ABSTRACT

We present the analysis of *ASCA* archival data from the Galactic source W51. The *ASCA* spectra show that the soft ( $kT \lesssim 2.5$  keV) X-rays are of thermal origin and are compatible with W51C being a single, isothermal ( $kT \simeq 0.3$  keV) supernova remnant at the far-side of the Sagittarius arm. The *ASCA* images reveal hard ( $kT \gtrsim 2.5$  keV) X-ray sources which were not seen in previous X-ray observations. Some of these sources are coincident with massive star-forming regions and the spectra are used to derive X-ray parameters. By comparing the X-ray absorbing column density with atomic hydrogen column density, we infer the location of star-forming regions relative to molecular clouds. There are unidentified hard X-ray sources superposed on the supernova remnant and we discuss the possibility of their association.

*Subject headings:* ISM: individual (W51) — supernova remnants — H II regions — stars: formation — X-rays: ISM

## 1. INTRODUCTION

W51 is an extended ( $\sim 1^\circ$ ) radio source located at the tangential point ( $l = 49^\circ$ ) of the Sagittarius arm. It is composed of two complex H II regions, W51A and W51B, and the supernova remnant (SNR) W51C (e.g., Bieging 1975; Koo 1997). W51A forms the northern part of W51, and is separated from the other two sources. It contains two major components, each composed of several compact H II regions. W51B is composed of at least six compact H II regions scattered over an area of  $\sim 15'$  size. W51B sources are associated with a stream of atomic and molecular gases, with line-of-sight velocities significantly greater than the maximum velocity permitted by Galactic rotation alone. The stream is thought to be gas flowing along the Sagittarius spiral arm in response to the perturbation due to the spiral potential (e.g., Burton 1971). Superimposed on W51B, there is an extended structure W51C

which is a SNR. W51C appears in radio continuum as an incomplete shell of  $\sim 30'$  extent with its upper portion open (Copetti & Schmidt 1991; Subrahmanyan & Goss 1995). Shocked atomic and molecular gases have been detected in the western part of the SNR, which indicates that the SNR is interacting with a large molecular cloud (Koo & Heiles 1991; Koo & Moon 1997a,b). The complex structure of W51 is partly due to the inclination of the Sagittarius arm, so that we look down the length of the arm a distance of 5 kpc along the line-of-sight.

Soft ( $\lesssim 2$  keV) X-ray emission associated with W51 has been detected by *Einstein* and ROSAT (Seward 1990; Koo et al. 1995, hereafter KKS). Diffuse X-rays come from a region surrounding W51B and W51C, whereas W51A has essentially no soft X-ray emission associated with it. The soft X-ray emitting region is elongated ( $50' \times 38'$ ) along the east-west direction, and may be divided into three parts; a central structure composed of

two bright regions separated by  $\sim 10'$ , an incomplete shell  $\sim 30'$  long in the east, and an extended ( $\sim 20' \times 10'$ ) structure in the west. The structure in the west is separated from the central region by a region of weak emission where molecular clouds associated with the W51B star-forming region are located. The systematic hardening of the X-ray spectrum toward the west suggested that the X-rays are emitted behind these molecular clouds. The average X-ray spectrum of the SNR was fitted well by a single-temperature ( $k_B T \simeq 0.29$  keV) thermal plasma model. But the energy range of the ROSAT detector was not enough to distinguish this from other emission models.

In this paper, we present the results of an *ASCA* study of the W51 complex. The greater (0.7–10 keV) energy coverage of *ASCA* makes it clear that the X-ray emission from the SNR is of thermal origin. The newly derived plasma parameters are consistent with the ROSAT results. *ASCA* also reveals hard X-rays from star-forming regions in W51, which were not seen by ROSAT.

## 2. *ASCA* Data and Image Processing

W51 was observed by *ASCA* October 10, 1995. Two chips of each SIS detector were aligned in 2-CCD mode to cover the bright central region revealed by ROSAT, while the GIS detector covered most of the X-ray emitting region. Figure 1 shows the positions of SIS and GIS fields overlaid on the ROSAT image of KKS. The data used are the archive data processed by the revision 2 standard screening process. The total exposure times after screening were 36.4 ks and 12.8 ks for SIS0 and SIS1, and 44.3 ks for both GIS2 and GIS3.

For spatial analysis, we have generated GIS images in the energy bands: 0.7–1.5 keV, 1.5–2.5 keV, 2.5–6.0 keV, and 6.0–10.0 keV. We first generated a raw GIS image for a given energy band and divided it by the blank-sky GIS image of the same energy band. The blank-sky image represents the response of X-ray telescope (XRT) plus GIS for uniform background emission. Therefore, by dividing the raw image by the blank-sky image, the background level in the image could be flattened (e.g., Kaneda 1998), and by subtracting a constant, a background-subtracted image was obtained. For a test, we applied the technique to a source-free region at  $\ell \simeq 50^\circ$  and confirmed

that the residual image did not have any systematic gradient. The vignetting effect for spatially-confined sources, however, is greater than that for the background because there is no stray-light coming from outside the field-of-view. We therefore divided the above image by an effective exposure map which accounts for the variation of effective area with detector position and energy. We constructed GIS2 and GIS3 images separately and added the two after masking out regions near the edge of the field and around the built-in calibration source. The images have pixel size of  $15'' \times 15''$  and have been smoothed using a Gaussian profile of  $\sigma = 1'$ . The count rates in the GIS2+3 images of 0.7–1.5, 1.5–2.5, 2.5–6.0, and 6.0–10.0 keV are 0.51, 0.64, 0.46, and 0.26 counts  $\text{s}^{-1}$ , respectively. Images of wider energy bands, e.g., 0.7–2.5 keV, were constructed by adding the above images. We generated SIS images in a similar way, except that they were not divided by blank-sky images because the background intensity was uniform over the field. SIS images have pixel size of  $6''.4 \times 6''.4$  and have been smoothed using a Gaussian profile of  $\sigma = 25''$ .

## 3. Spatial Analysis

### 3.1. *ASCA* Images

#### 3.1.1. GIS Images

Figure 2a is GIS image of W51 in the total (0.7–10.0 keV) energy band and shows that the region has a complex X-ray morphology. This is partly due to the superposition of unrelated sources, which can be distinguished by looking at soft and hard X-ray images. Figures 2b and 2c are GIS images of W51 in the soft (0.7–2.5 keV) and hard (2.5–6.0 keV) energy bands. Figure 2b, which is consistent with the ROSAT image of KKS (Fig. 1), shows an extended structure  $\sim 20'$  long along the SE-NW direction at the field center. It is composed of two bright regions, regions XN and XS, separated by  $\sim 10'$ . XS has a ridge extending to the east. There is also a bright extended structure in the west, XW. These structures are immersed in fainter diffuse emission.

In hard X-rays (Fig. 2c), there are also bright regions and faint diffuse emission. The bright regions are small and could be unresolved sources. Some of the diffuse emission might be instrumen-

tal because the point spread function of the *ASCA* XRT has a broad wing. Excluding emission at the edge of the field, we identify three sources. Two of them (HX1 and HX3) are somewhat extended and might have more than one component; in HX1, there appears to be a structure to the southeast of the maximum, while HX3 appears double. Sources HX2 and HX3 are located close to regions XS and XN, respectively, and the deformation of the contours in Figure 2b corresponds to these hard sources. Table 1 summarizes source properties. HX3-east and HX3-west represent the east and west components of HX3, respectively. The peak positions and count rates are derived from Figure 2c. The positional uncertainty is  $\sim 1'$ . The count rates are uncertain ( $\gtrsim 20\%$ ) because of background subtraction, confusion with other sources, and the vignetting correction. The last four columns summarize the properties of the radio counterparts (see § 3.2).

Figure 2d is an X-ray color map generated from three energy bands: 0.7–1.5 keV (red), 1.5–2.5 keV (green), and 2.5–6.0 keV (blue), and offers an alternate way to look at this region. The soft sources in Figure 2b appear with different colors, regions XN and XS in yellow, region XW in green, and the faint features in the southeast in red. This illustrates the result of KKS who found that the X-ray spectrum between 0.6 keV and 2.2 keV becomes systematically harder toward the west. As will be shown in § 3.3, this is probably due to the absorption of intervening interstellar gas. The hard X-ray sources of Figure 2c appear blue in Figure 2d.

### 3.1.2. SIS Images

Figures 3a and 3b are the soft and hard SIS images of the central region of W51 (cf. Fig. 1). These have higher ( $\sim 1'$ ) resolution and show more structure. In order to help compare Figures 2 and 3, we mark the peak positions in Figures 2b and 2c as crosses in Figures 3a and 3b, respectively. According to Figure 3a, the brightest part of region XN is elongated ( $\sim 3'$ ) eastwest, while the brightest part of region XS is resolved into northern and southern components. In Figure 3b, HX2 is visible in the southern area while HX3-east is barely visible near the northwestern boundary. HX2 and the southern component of XS are both elongated eastwest and partly overlap, which suggests that

they might be the same source.

## 3.2. Comparison with Radio Distribution

An overlay of X-ray and radio images helps to understand this complex region. Figure 4a compares the ROSAT X-ray image of KKS with a radio contour map. This ROSAT image contains almost the same information as the *ASCA* soft X-ray map but covers a larger area. KKS did a similar comparison, but the radio maps that they used either had poor angular resolution (FWHM=4.2') or did not show large-scale ( $\gtrsim 15'$ ) structures. Figure 4a uses the 330 MHz map of Subrahmanyan & Goss (1995) which shows the detailed ( $\sim 1'$ ) structures over the whole complex. In Figure 4a, the clusters of compact sources in the north and near the center are known as the W51A and W51B H II region complexes, respectively. The W51C SNR appears as an incomplete, very thick radio shell in the southeast. The eastern X-ray shell matches almost perfectly with the outer boundary as expected for a SNR. Regions XN and XS are partly surrounded by the radio shell, and they appear to be immersed in a diffuse X-ray emission together with the eastern X-ray shell. This might indicate that they are parts of the SNR too. SNRs with centrally-brightened X-ray emission are not unusual (see § 5.1). On the other hand, the western half of the SNR is not clearly defined in radio because of the superimposed source W51B. But the western edge of the radio source is also matched in X-ray emission with region XW. This probably shows the western shell of the SNR. In § 4.1, we will show that regions XN, XS, and XW are all located at the far-side of the Sagittarius arm and have similar temperatures, which suggests that they are all possibly parts of a single SNR.

Figure 4b compares the hard X-ray image with the radio image and shows that some of the hard X-ray sources are associated with compact radio sources. First, HX1 coincides with G48.9–0.3 and G49.0–0.3 which are compact H II regions. Second, HX3-east coincides with G49.2–0.3, also a compact H II region. Third, the bright X-ray source at the northern boundary of the *ASCA* field might be associated with W51A which is mostly outside the field of view. The hard X-rays from these sources, therefore, might originate from early-type stars and young stellar objects.

For HX2 and HX3-west, there are no obvious corresponding radio sources in Figure 3b, although there seems to be a weak enhancement at HX2. We examined the image of the NRAO VLA Sky Survey (NVSS) at 21 cm (Condon et al. 1988) and found that there are indeed weak radio sources coincident with these hard X-ray sources too. The nature of these radio sources is unknown. The results of the comparison are summarized in Table 1.

### 3.3. Comparison with CO Distribution

KKS compared the distribution of ROSAT X-ray surface brightness with that of CO and concluded that the spectral hardness between 0.6–2.2 keV was due to the absorption of X-ray photons by intervening interstellar gas. There is now more sensitive CO data with higher spatial resolution. Figure 5a compares the ROSAT X-ray image with the CO J=1–0 integrated-intensity map generated from the data of Carpenter & Sanders (1998). The CO map is obtained integrating over the velocity range of 0 to +75 km s<sup>-1</sup> and shows all the molecular gas toward this direction. The CO map has an angular resolution of  $\simeq 45''$  with  $50''$  sampling. W51A is associated with the bright CO cloud in the northern part of the field, while the W51B radio sources are associated with a filamentary cloud in the central field. (For a detailed comparison of radio sources and molecular clouds in W51B, see Koo [1999].)

Figure 5a strongly suggests that the spectral hardening in soft X-rays is due to the absorption of the intervening interstellar gas. First there is generally more molecular gas toward region XW than regions XN and XS. Second, the central filamentary cloud partly overlaps with the western boundary of region XN where the spectrum is harder (Fig. 2d). If we use  $N_{\text{H}_2}/W_{\text{CO}} = 2.3 \times 10^{20}$  molecules cm<sup>-2</sup> (K km s<sup>-1</sup>) where  $W_{\text{CO}}$  is the integrated CO J=1–0 line intensity in K km s<sup>-1</sup> and  $N_{\text{H}_2}$  (cm<sup>-2</sup>) is the molecular hydrogen column density (Strong et al. 1988), then, the average H<sub>2</sub> column densities toward regions XW, XN, and XS are 0.54, 0.45, and  $0.20 \times 10^{22}$  cm<sup>-2</sup>, respectively. The H I column density is also somewhat greater toward the west, e.g., 1.6, 1.5, and  $1.4 \times 10^{22}$  cm<sup>-2</sup> toward XW, XN, and XS. As will be shown in § 4.1, the spectra of the three regions require different absorbing column densities of hydrogen nuclei and this result is consistent with the X-rays com-

ing from behind most of the atomic and molecular gases. The red color of the southeastern X-ray shell in Figure 2d is consistent with the negligible CO emission and smaller ( $1.2 \times 10^{22}$  cm<sup>-2</sup>) H I column density in this direction.

Figure 5a also shows that the central filamentary molecular cloud appears to fill the gap between the central and the western X-ray emitting regions (see Koo [1999] for a detailed structure of this cloud.). KKS examined their correlation and concluded that the column density of the cloud is large enough to produce the dip, but, because we see soft X-rays at the northwestern boundary of XN toward which  $N_{\text{H}}$  is comparable, the intrinsic brightness in the dip must be fainter than the central region. According to Figure 5a, there are regions of low soft X-ray emission in the dip where the CO emission is rather weak, and this might be another evidence suggesting that the intrinsic soft X-ray brightness in the dip is faint.

On the other hand, Figure 5b shows that the X-ray sources HX1 and HX3-east are associated with molecular clouds, which is consistent with these sources being compact H II regions. HX2 and HX3-west are not associated with CO emission, which suggests that they might be either background sources or sources associated with the SNR. (The contour surrounding HX3-west in Figure 5b represents a minimum.)

## 4. Spectral Analysis

As we have seen in § 3, W51 is a complex region with X-rays coming from a SNR, star-forming regions, and perhaps background sources. In this section, we first inspect the spectra of regions bright in soft X-ray, which are considered to be the parts of the SNR W51C. We then inspect the spectra of hard X-ray sources, some of which are star-forming regions and some are unidentified.

### 4.1. W51C SNR

#### 4.1.1. GIS spectra

Figure 6 shows the spectra of regions XN, XS, and XW. Each spectrum is obtained by adding all the photons within the corresponding area marked in Figure 2b and by subtracting a background spectrum. The background spectrum in each region was estimated from the source-free region in

the northern part of the field. There are several points to be made from Figure 6. First, the spectra clearly show line features at  $\sim 1.3$  keV and  $\sim 1.8$  keV, which indicates that the emission is of thermal origin. The central energies of the line features are close to those of the K lines of He-like Mg and Si ions. Second, the spectra of regions XN and XS clearly have an excess emission at  $E \gtrsim 2.5$  keV compared to XW. This excess emission might be due to the hard X-ray sources HX2/HX3 but there is also the diffuse emission (Figure 2c). Third, at  $E \lesssim 2$  keV, the spectrum becomes harder in the order of regions XS, XN, and XW, which is consistent with Figure 2d.

We first tried to fit the spectrum with a single-temperature, equilibrium thermal emission model. The fitting was done using the MEKAL code inside the XSPEC package (version 10). The data between  $E = 0.7$  and  $6.0$  keV were used. Both the gas temperature  $T$  and the absorbing column density of hydrogen nuclei  $N_{\text{H}}$  were varied and the goodness of fit to the data was calculated. The elemental abundances were fixed to be solar. The fitting, however, was not satisfactory for all three regions. We therefore fitted a two-temperature equilibrium thermal model for regions XN and XS. For region XW, which has low S/N ratio, we instead limited the energy range to  $E = 0.7$ – $2.0$  keV. The parameter values that minimize  $\chi^2$  are taken as the “best fit”. The results are shown in Figures 6 and 7 and the best-fit parameters are listed in Table 2. (The quoted errors in Table 2 are 90% confidence limits calculated for one variable. Since  $N_{\text{H}}$  and  $kT$  are not independent, the range of values and coupling is better illustrated by the result of the joint analysis shown in Figure 7.) In the three regions, the soft components have significantly different  $N_{\text{H}}$ ,  $(1.9$ – $2.8) \times 10^{22} \text{ cm}^{-2}$ , but similar temperatures ( $kT \simeq 0.3$  keV). The different  $N_{\text{H}}$  are consistent with the variation of *total* column densities of hydrogen nuclei along these directions, which are listed in Table 2 for comparison. In Table 2,  $N_{\text{HI}}$  is HI column density derived using *colden* (a program provided by *Chandra* X-ray center to compute total Galactic HI column densities based on the compilation by Dickey & Lockman [1990]), while  $N_{\text{H}_2}$  is  $\text{H}_2$  column density derived from the CO data described in § 3.2. The agreement between the X-ray absorbing column densities and the observed total column densities

is very good. Therefore, we conclude that the three regions appear to be behind most of atomic and molecular gases in the Sagittarius arm.

The parameters of the hard components in regions XN and XS are poorly defined. Only the temperatures can be said to be an order-of-magnitude higher than the low-temperature component. Indeed, the hard X-rays probably originate from sources with different characteristics and the parameters in Table 2 should not be taken at face value. But the parameters of the soft component in Table 2 are not sensitive to which model used for the hard energy part. We will explore the spectral properties of the hard X-ray sources in § 4.2.

#### 4.1.2. SIS Spectra

SIS has higher energy resolution and can be used to determine accurate parameters of emission lines. However, in W51, the superposition of hard X-ray sources and the absence of a ‘clean’ background make the analysis difficult. We therefore limit the analysis to broadband model fitting. Figure 8 shows the SIS spectra of regions XN and XS. The areas used to derive the spectra are marked as solid circles in Figure 3a and do not include compact hard X-rays sources. The background spectra were estimated from relatively emission-free regions in the field. We fit a single-temperature, equilibrium thermal model to the spectrum of XN between  $E = 0.7$  and  $2.5$  keV, because, at higher energies, there is a contamination by diffuse hard X-ray emitting gas. We obtain  $N_{\text{H}} = 2.60^{+0.23}_{-0.24} \times 10^{22} \text{ cm}^{-2}$  and  $kT = 0.25^{+0.05}_{-0.03}$  keV ( $\chi^2 = 50/39$ ) and the result is shown in Figure 8. The temperature agrees with that derived from the GIS spectrum, while the absorbing column density is a little larger. Similarly, for region XS, we obtain  $N_{\text{H}} = 1.98 \pm 0.22 \times 10^{22} \text{ cm}^{-2}$  and  $kT = 0.34^{+0.09}_{-0.06}$  keV ( $\chi^2 = 30/23$ ) in agreement with the result from the GIS spectrum.

### 4.2. Hard X-ray Sources

#### 4.2.1. HX1

HX1 is an extended source associated with compact H II regions. Figure 9 shows the spectrum of HX1. The background emission was estimated from a source-free region in the southern part of the field. The spectrum of HX1 has an indica-

tion of Si K line at  $\sim 2.0$  keV (and perhaps S K line at  $\sim 2.4$  keV), which, together with the geometrical coincidence with the compact H II regions, suggests that it is of thermal origin. We fit a single-temperature, equilibrium thermal model to the energy band  $E = 0.7\text{--}8.0$  keV. The result is shown in Figure 9 and the best-fit parameters are summarized in Table 3. In Table 3,  $F_X$  and  $L_X$  are the X-ray flux and X-ray luminosity between  $E = 0.7$  and  $10.0$  keV.

#### 4.2.2. HX2

HX2 is unidentified. The absence of CO emission suggests that it is either a background source or possibly a source associated with the SNR W51C, e.g., a pulsar synchrotron nebula. Figure 10 shows the GIS and SIS spectra of HX2. The soft-energy spectra include a contribution from the emission of the SNR. The contamination might be smaller for the SIS spectrum because the instrument has a sharper point spread function and the spectrum was extracted from a region chosen to encompass only HX2. (For the areas used to extract the spectra, see Figures 2c and 3b.) The GIS spectrum, on the other hand, has a higher signal-to-noise ratio in the hard energy band. We simultaneously fit the GIS and SIS spectra with two components, i.e., soft and hard components representing the emissions from the SNR and HX2, respectively. The soft component is assumed to be thermal and its parameters are fixed for those of region XS in Table 2. For the hard component, we consider both power-law and thermal emission models, but their absorbing column densities are assumed to be equal to that of XS ( $1.86 \times 10^{22} \text{ cm}^{-2}$ ), which is also equal to the total column density in this direction. This implicitly assumes that HX2 is either a background source or a source associated with the SNR. Even if not, the derived photon index and plasma temperature are not sensitive to absorbing column density. Both models can fit the spectra with comparable statistical significance, and Table 3 summarizes the results. The power-law result is plotted in Figure 10.

#### 4.2.3. HX3

HX3 includes two point-like sources: HX3-east associated with a compact H II region and HX3-west which is unidentified. Figure 11 shows the

GIS and SIS spectra of HX3. The area used to extract the GIS spectrum includes both HX3-east and HX3-west, while the area for the SIS spectrum includes only HX3-east (see Figures 2c and 3b). We therefore fit the GIS and SIS spectra with three and two components, respectively. Two components for the SIS spectrum are the soft and hard components representing the emissions from the SNR and HX3-east, respectively. For the GIS spectrum, we add one more component representing the hard X-ray emission from HX3-west. Because of low S/N ratio, however, we want to fix the parameters of these components as much as possible. First in § 4.1, we found that the SNR is probably at the far side of the Sagittarius arm. The column density toward the compact H II region associated with HX3-east is also large (see § 5.2). We do not have any information for HX3-west, but it is possibly a background source. We therefore fix the X-ray absorbing column density toward all the components for  $N_H = 3.0 \times 10^{22} \text{ cm}^{-2}$ , which is the total column density in this direction. We adopt the best-fit temperature (0.29 keV) of region XN as the temperature of the SNR emission. The emission from HX3-east is assumed to be thermal because it is associated with a compact H II region. For HX3-west, we just consider power-law emission model. The results are shown in Figure 11 and Table 3. The three-component fit to the GIS spectrum is, of course, not unique but results are consistent with our analysis of the region.

## 5. DISCUSSION

### 5.1. W51C SNR

According to our results, most parts of W51C emit X-rays from hot gas at a temperature of  $\simeq 0.3$  keV. (The temperature of the faint region along the southeastern boundary of the GIS field is consistent with this too, i.e.,  $kT = 0.18^{+0.19}_{-0.07}$  keV, although it has a large uncertainty.) The possibility of the central X-ray emission being largely a synchrotron nebula, as considered by KKS, is ruled out. Furthermore, since the absorbing columns toward the X-ray emitting regions are approximately equal to the total column densities of hydrogen nuclei in those directions, the X-rays probably originate behind most of the atomic and molecular gas in the Sagittarius arm. The *ASCA* results therefore are compatible with W51C be-

ing a single, isothermal SNR at the far side of the Sagittarius arm.

At a distance of 6 kpc, the linear extent of W51C is  $88 \times 66$  pc, which makes it one of the largest SNRs in the Galaxy (e.g., Strom 1996). We have derived the parameters of the central region; an elliptical ( $23' \times 15'$ ) area surrounding regions XN and XS. The root mean, volume-averaged, square density  $\bar{n}_e \equiv (\int n_e^2 dV/V)^{1/2} \simeq 0.58 \text{ cm}^{-3}$ , the X-ray emitting mass  $M_X \simeq 290 M_\odot$ , and the thermal energy  $E_{\text{th}} \simeq 0.39 \times 10^{51}$  ergs. For comparison, KKS derived  $\bar{n}_e \simeq 0.29 \text{ cm}^{-3}$ ,  $M_X \simeq 1900 M_\odot$ , and  $E_{\text{th}} \simeq 2.6 \times 10^{51}$  ergs for the whole ( $50' \times 38'$ ) SNR. If the X-ray emitting gas is clumpy with a volume filling factor of  $f$ , the true electron density  $n_e$  would be greater by a factor of  $f^{-1/2}$ , whereas the X-ray emitting mass would be smaller by a factor of  $f^{1/2}$ . Thermal energy could be greater ( $f^{-1/2}$ ) or smaller ( $f^{1/2}$ ) depending on whether the interclump region is filled for the SNR to be isobaric or not. From the *Einstein* image (Fig. 1), we estimate that the volume filling factor of the X-ray emitting gas  $f \lesssim 0.4$  for the whole SNR, so that  $n_e \gtrsim 0.46 \text{ cm}^{-3}$ ,  $M_X \lesssim 1200 M_\odot$ , and  $E_{\text{th}} \gtrsim 4.1 \times 10^{51}$  ergs or  $E_{\text{th}} \lesssim 1.6 \times 10^{51}$  ergs. KKS estimated the age of the SNR at  $\sim 3 \times 10^4$  yrs.

As a single SNR, W51C has a composite morphology: a very thick ( $\sim 13'$  or 23 pc) outer radio and X-ray shell and an X-ray-bright central region. There are about 15 other composite SNRs, corresponding to  $\sim 25\%$  of X-ray-detected Galactic SNRs (Rho & Petre 1998). Several models have been suggested, which include the evaporation cloud model of White & Long (1991) and the heat conduction model of Shelton et al. (1999). The former assumes small dense clouds evaporating within the hot interior, while the latter considers only heat conduction within the hot interior. Observationally, many of these SNRs are known to be interacting with large molecular clouds (see Rho & Petre 1998 and references therein). It has been shown that W51C is interacting with a molecular cloud along the western boundary of region XN (Koo & Moon 1997b), and some, if not all, of the X-ray emitting gas in the central area could have been originated from this molecular cloud.

Since W51C is located in the Sagittarius arm and is interacting with a molecular cloud, is likely to be a type II SNR. According to our results,

however, most of the soft X-ray emission in the central region is thermal, certainly not consistent with a bright pulsar wind nebula. Among hard X-ray sources, HX2 and HX3-west are unidentified and could be candidates for a weak pulsar nebula. Their spectra can be fitted by a power-law model with  $\Gamma = 2.59_{-0.29}^{+0.27}$  and  $1.7_{-\infty}^{+1.0}$  (or  $\lesssim 2.7$ ), respectively, although they can be fitted equally well by a thermal emission model. These photon indices fall into the range (1.6–2.5) of the indices of known pulsar nebulae (Seward & Wang 1988). If we extrapolate their spectra to low energies by the same power law, their X-ray luminosities in the *Einstein* band (0.2–4 keV) would be  $\sim 0.4\text{--}2 \times 10^{34} \text{ ergs s}^{-1}$  assuming  $d = 6$  kpc. This is  $\lesssim 0.1\%$  of Crab nebula and is not unreasonable as a luminosity of a  $\sim 3 \times 10^4$  yrs old pulsar (Seward & Wang 1988). Recent *Chandra* discoveries also indicate that many young pulsars and pulsar wind nebulae do not have high luminosities (Olbert et al. 2001; Hughes et al. 2001). High spatial resolution is needed in order to explore the nature of these sources and to look for a faint pulsar and its nebula.

## 5.2. X-ray emission from W51 star-forming regions

We have detected hard X-ray sources coincident with several compact H II regions in W51. The *ASCA* hard image (Fig. 2c) implies that W51A might be the brightest hard X-ray source among the W51 star-forming regions, but the source is located at the edge of the GIS field and its properties could not be obtained. Among the W51B sources, two compact H II regions, G48.9–0.3 and G49.0–0.3, are coincident with the brightest hard X-ray source HX1. The brightest radio continuum source in W51B, G49.2–0.3, is also detected as HX3-east, but is much fainter. These X-rays might be from early-type stars and young stellar objects in these compact H II regions.

Recent *Chandra* observation of the Orion Trapezium region showed that the X-rays are mostly from individual OB stars (Schulz et al. 2001). The three brightest stars,  $\theta^1$  Ori A, C, & E, of spectral type O7–B0.5 have  $L_X = (2\text{--}19) \times 10^{31} \text{ erg s}^{-1}$  and account for more than 80% of the total luminosity of the Trapezium. Stars of later spectral type are much fainter. The X-ray luminosity of HX1 is  $1.6 \times 10^{34} \text{ erg s}^{-1}$ , an order of

magnitude greater than that of the Orion star-forming region (Feigelson 2000). According to Han (2001), who analyzed the *2MASS* data of W51B to derive stellar populations of compact H II regions, G48.9–0.3 and G49.0–0.3 together have 3 O-type stars (O6.5, O8, and O9), 8 B0 stars, and 13 B1 stars and these do not seem to be enough to account for the observed X-ray luminosity. It is possible that there are OB stars unidentified from the *2MASS* data and/or some diffuse emission. The *Einstein* observations of the Carina Nebula showed that 80% of the X-ray emission came from a diffuse component (Seward & Chlebowski 1982). Alternatively, the OB stars in these compact H II regions could be brighter in X-rays than those in Orion. The X-ray luminosity of O-stars does seem to depend on their surroundings (Chlebowski 1989). We need high-resolution X-ray observations to find out the sources of X-rays in these compact regions.

One important result of the X-ray study is that we can determine the locations of compact H II regions within molecular clouds. The X-ray absorbing column density toward HX1 ( $N_{\text{H}} \simeq 1.5 \times 10^{22} \text{ cm}^{-2}$ ) is not very much greater than the column density of *atomic* hydrogen to the associated compact H II regions, i.e.,  $N_{\text{HI}} = (1.23\text{--}1.50) \times 10^{22} \text{ cm}^{-2}$  (Koo 1997). Therefore, if we assume that most of the X-rays are from these H II regions, our result implies that the H II regions are in the front side of the molecular cloud. This is consistent with the result of Han (2001). They found that the extinction toward exciting stars in G48.9–0.3 and G49.0–0.3 corresponds to  $A_V \simeq 8$ , which agrees very well with our X-ray absorbing column density if we consider  $N_{\text{H}}/A_V \simeq 1.8 \times 10^{21} \text{ cm}^{-2} \text{ mag}^{-1}$  (Seward 2000). For HX3-east, however, instead of deriving an X-ray absorbing column density from a model fitting, we adopted total, i.e., atomic and molecular, hydrogen column density because of the uncertainty due to other superposed sources. According to Han (2001), G49.2–0.3 associated with HX3-east is located in the back side of the molecular cloud.

## 6. CONCLUSIONS

W51 is a complex region with a SNR and star-forming regions superposed within an area of angular diameter  $\sim 1^\circ$ . Soft X-rays from the SNR

were detected by *Einstein* and ROSAT, but, because of the limited energy range of detector, it was not conclusive whether the emission was thermal or non-thermal. The *ASCA* study in this paper clearly shows that most parts of the SNR emit thermal X-rays and the temperature of the hot gas is about 0.3 keV. It also shows that the X-rays originate behind most of the atomic and molecular gas along those line of sights. These results are compatible with X-rays being emitted from a single, isothermal SNR at the far-side of the Sagittarius arm, which makes the W51C SNR one of the largest SNRs in the Galaxy.

The *ASCA* observations reveal hard X-rays from the W51B star-forming regions. Two regions (G48.9–0.3 and G49.0–0.3) appear bright in hard X-rays and it is likely that they are located in the front side of the molecular cloud. W51 is a rare example of a SNR superposed on a star-forming region. Since the progenitors of Type II SN are massive stars, this situation should be more common, but it is not. Apparently W51 is one of those few regions in the Galaxy where we can study the formation of massive stars and the consequence of their violent explosions simultaneously. High-resolution X-ray observations are needed to fully identify the origins of the central emission.

We are grateful to Miller Goss, Ravi Subrahmanyam, and John Carpenter for providing their H I and CO data for comparison with the *ASCA* data. We wish to thank Nancy Brickhouse for providing a list of strong lines in X-rays. We also wish to thank the anonymous referee for helpful comments. BCK wish to thank Chul-Sung Choi for helpful discussions. JJL would like to thank the Ministry of Education for its financial support. This work was supported by the Korea Research Foundation Grant (KRF-2000-015-DP0446).



## REFERENCES

- Bieging, J. 1975, in *H II Regions and Related Topics*, ed. T. L. Wilson & D. Downes (Heidelberg: Springer-Verlag), 443
- Burton, W. B. 1971, *A&A*, 10, 76
- Carpenter, J. M., & Sanders, D. B. 1998, *AJ*, 116, 1856
- Chlebowski, T. 1989, *ApJ*, 342, 1091
- Condon, J. J., et al. 1988, *AJ*, 115, 1693
- Copetti, M. V. F., & Schmidt, A. A. 1991, *MNRAS*, 250, 127
- Dickey, J. M., & Lockman, F. J. 1990, *ARAA*, 28, 215
- Feigelson, E. D. 2000, astro-ph/0012486
- Han, S. W. 2001, Master thesis
- Hughes, J. P., Slane, P. O., Burrows, D. N., Garmire, G., & Nousek, J. N. 2001, astro-ph/0106031
- Kaneda, H., Makishima, K., Yamauchi, S., Koyama, K., Matsuzaki, K., & Yamasaki, N. Y. 1997, *ApJ*, 491, 638
- Koo, B.-C. 1997, *ApJS*, 108, 489
- 1999, *ApJ*, 518, 760
- Koo, B.-C., & Heiles, C. 1991, *ApJ*, 382, 204
- Koo, B.-C., Kim, K.-T., & Seward, F. D. 1995, *ApJ*, 447, 211 (KKS)
- Koo, B.-C., & Moon, D.-S. 1997a, *ApJ*, 475, 194
- 1997b, *ApJ*, 485, 263
- Olbert, C. M., Clearfield, C. R., Williams, N. E., Keohane, J. W., & Frail, D. A. 2001, *ApJL*, 554, L205
- Rho, J., & Petre, R. 1998, *ApJL*, 503, L167
- Schulz, N. S., Canizares, C., Huenemoerder, D., Kastner, J. H., Taylor, S. C., & Bergstrom, E. J. 2001, *ApJ*, 549, 441
- Seward, F. D. 1990, *ApJS*, 73, 781
- 2000, in *Allen's Astrophysical Quantities*, ed. A. Cox (AIP Press), 197
- Seward, F. D., & Chlebowski, T. 1982, *ApJ*, 256, 530
- Seward, F. D., & Wang, Z. 1988, *ApJ*, 332, 199
- Shelton, R. L., Cox, D. P., Maciejewski, W., Smith, R. K., Plewa, T., Pawl, A., & Różyczka, M. 1999, *ApJ*, 524, 192
- Strom, R. G. 1996, in *IAU Colloq. 145, Supernovae and Supernova Remnants*, ed. R. McCray & Z. Wang (Cambridge: Cambridge Univ. Press), 333
- Strong et al. 1988, *A&A* 207, 1
- Subrahmanyan, R., & Goss, W. M. 1995, *MNRAS*, 275, 755
- White, R. L., & Long, K. S. 1991, *ApJ*, 373, 543

Fig. 1.— Position of *ASCA* SIS (squares) and GIS (circle) fields marked on the ROSAT image of Koo et al. (1995). Contour levels are linearly spaced from 10% to 80% of the peak brightness with steps of 10%. Peak brightness excluding the strong point source in the field is  $1.2 \times 10^{-4}$  counts  $\text{s}^{-1}$  pixel $^{-1}$ .

Fig. 2.— GIS2+3 images in the (a) 0.7–10.0 keV, (b) 0.7–2.5 keV, and (c) 2.5–6.0 keV energy bands. Background subtraction, vignetting correction, and exposure correction were made. Contour levels are linearly spaced from 20% to 90% of the peak brightness with steps of 10% in each map. Peak values are  $1.85$ ,  $1.47$ , and  $0.90 \times 10^{-4}$  counts  $\text{s}^{-1}$  pixel $^{-1}$ , respectively. The solid circles mark the areas used for spectral analysis. (d) X-ray color map generated from three energy bands; 0.7–1.5 keV (red), 1.5–2.5 keV (green), and 2.5–6.0 keV (blue).

Fig. 3.— SIS0+1 images in the (a) 0.7–2.5 keV and (b) 2.5–6.0 keV energy bands. Vignetting and exposure corrections were made. Contour levels are linearly spaced from 30% to 90% of the peak brightness with steps of 10% in each map. Peak values are  $0.17$  and  $0.24 \times 10^{-4}$  counts  $\text{s}^{-1}$  pixel $^{-1}$ , respectively. The crosses in (a) mark the peak positions of XN and XS in Figure 2b, while those in (b) mark the peak positions of HX2 and HX3-east in Figure 2c. The solid circle and ellipses mark the areas used for spectral analysis.

Fig. 4.— 330 MHz radio contour map of the W51 complex overlaid on the (a) ROSAT and (b) *ASCA* GIS hard (2.5–6.0 keV) X-ray images. The ROSAT X-ray map is used instead of the *ASCA* GIS soft X-ray image because it covers a larger area. The 330 MHz map is from Shurirahmanian & Goss (1995). In radio, W51 is composed of two complex H II regions, W51A and W51B, and the shell-type SNR W51C. Their approximate positions are marked in (a). Compact radio sources labeled in (b) are the W51B H II regions which are associated with hard X-ray sources.

Fig. 5.— Same as Figure 4, but with  $^{12}\text{CO}$  integrated intensity contour map. The CO map is obtained integrating over the velocity range of 0 to  $+75$   $\text{km s}^{-1}$  and shows all the molecular gas toward this direction. The contour levels (in K km

$\text{s}^{-1}$ ) are 20, 40, 60, 80, 100, 150, and 200. The column density of hydrogen nuclei corresponding to 1 K  $\text{km s}^{-1}$  is about  $4.6 \times 10^{20}$   $\text{cm}^{-2}$ . The CO maps are generated from the data of Carpenter & Sanders (1998).

Fig. 6.— GIS spectra of regions XN, XS, and XW. The solid lines show the best-fit equilibrium thermal emission models (MEKAL). For regions XN and XS, a two-temperature model was fit for  $E = 0.7$ –6.0 keV. For region XW, a single-temperature model was fit for  $E = 0.7$ –2.0 keV. Dashed lines show the contributions from individual components.

Fig. 7.— 90% confidence contours for the soft-component parameters of regions XN, XS, and XW.

Fig. 8.— Same as Figure 6, but for the SIS spectra of regions XN and XS.

Fig. 9.— GIS spectrum of HX1. The solid line shows the best-fit equilibrium, thermal emission model.

Fig. 10.— GIS and SIS spectra of HX2. The solid lines show the best-fit two component model with soft and hard components representing the emissions from the SNR and HX2, respectively. Dashed lines show the contributions from individual components.

Fig. 11.— GIS and SIS spectra of HX3. The SIS spectrum is fitted with two components with soft and hard components representing the emission from the SNR and HX3-east, respectively. For the GIS spectrum, we added one more component (dotted line) representing HX3-west.

TABLE 1  
PROPERTIES OF HARD X-RAY SOURCES

Source	Peak Position ( $\alpha_{2000}$ , $\delta_{2000}$ )	Count Rates <sup>a</sup> ( $\times 10^{-2}$ counts s <sup>-1</sup> )	Radio Counterpart			
			Source	( $\alpha_{2000}$ , $\delta_{2000}$ )	21-cm Flux Density (Jy)	Reference
HX1	(19 22 21, 14 05 30)	4.3	G48.9-0.3	(19 22 14.2, 14 02 57)	4.02	1
			G49.0-0.3	(19 22 25.7, 14 06 18)	1.23	1
HX2	(19 23 17, 14 02 50)	1.1	unidentified	(19 23 18.3, 14 02 31)	0.093	2
HX3-east	(19 23 02, 14 16 30)	0.8	G49.2-0.3	(19 23 01.3, 14 16 50)	7.42	1
HX3-west	(19 22 47, 14 16 20)	1.0	unidentified	(19 22 45.5, 14 16 06)	0.024	2

<sup>a</sup>Between  $E = 2.5$  and 6.0 keV.

REFERENCES.—(1) Koo 1997; (2) Condon et al. 1998.

TABLE 2  
SPECTRAL ANALYSIS OF THE REGIONS BRIGHT IN SOFT X-RAYS

Region	Soft Component		Hard Component		$\chi^2$	Atomic and Molecular Columns		
	$N_{\text{H}}$ ( $10^{22} \text{ cm}^{-2}$ )	$kT$ (keV)	$N_{\text{H}}$ ( $10^{22} \text{ cm}^{-2}$ )	$kT$ (keV)		$N_{\text{HI}}$ ( $10^{22} \text{ cm}^{-2}$ )	$2N_{\text{H}_2}$ ( $10^{22} \text{ cm}^{-2}$ )	$N_{\text{HI}} + 2N_{\text{H}_2}$ ( $10^{22} \text{ cm}^{-2}$ )
XN	$2.25^{+0.20}_{-0.17}$	$0.29^{+0.06}_{-0.05}$	$1.8^{+1.9}_{-1.2}$	$2.5^{+2.0}_{-0.8}$	111/102	1.5	0.9	2.4
XS	$1.86^{+0.38}_{-0.22}$	$0.34^{+0.05}_{-0.06}$	$\lesssim 4.4$	$\gtrsim 2.4$	78/92	1.4	0.4	1.8
XW	$2.8^{+0.9}_{-0.6}$	$0.29^{+0.14}_{-0.10}$	...	...	29/23	1.6	1.1	2.7

TABLE 3  
SPECTRAL ANALYSIS OF HARD X-RAY SOURCES

Source	Emission Model	$N_{\text{H}}$ ( $10^{22} \text{ cm}^{-2}$ )	$kT$ (keV)	$\Gamma$	$F_X^{\text{a}}$ ( $10^{-12} \text{ ergs cm}^{-2} \text{ s}^{-1}$ )	$L_X^{\text{a,b}}$ ( $10^{34} \text{ ergs s}^{-1}$ )
HX1	thermal	$1.45^{+0.31}_{-0.30}$	$3.3^{+1.1}_{-0.6}$	...	5.5	1.6
HX2	power-law	$1.86^{\text{c}}$	...	$2.59^{+0.27}_{-0.29}$	2.1	0.89
	thermal	$1.86^{\text{c}}$	$2.6^{+0.6}_{-0.4}$	...	1.6	0.69
HX3-east	thermal	$3.0^{\text{c}}$	$\lesssim 3.0^{\text{d}}$	...	1.5	0.45
HX3-west	power-law	$3.0^{\text{c}}$	...	$\lesssim 2.7^{\text{d}}$	1.2	0.52

<sup>a</sup>Between  $E = 0.7$  and  $10.0$  keV.

<sup>b</sup>HX1 and HX3-east are associated with compact H II regions in W51B and their distances are assumed to be 5 kpc. HX2 and HX3-west are unidentified sources and their distances are assumed to be 6 kpc.

<sup>c</sup>These are fixed.

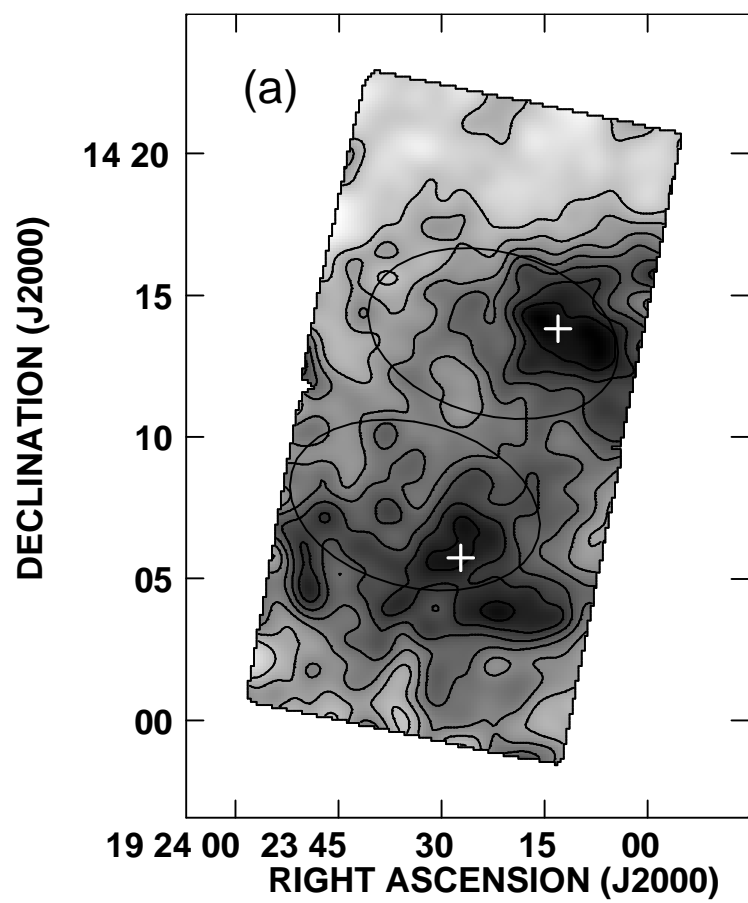
<sup>d</sup>These parameters do not have a lower bound for the 90% confidence interval.  $F_X$  (and  $L_X$ ) of HX3-east and HX3-west are based on the best-fit parameter values  $kT = 1.8$  keV and  $\Gamma = 1.7$ , respectively.

This figure "fig1.jpg" is available in "jpg" format from:

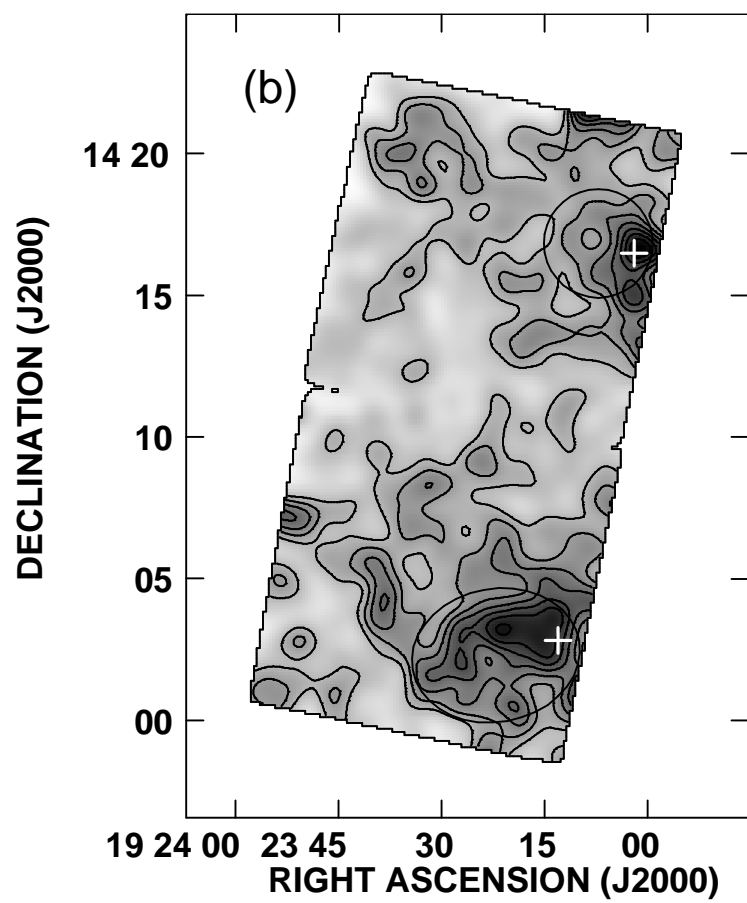
<http://arXiv.org/ps/astro-ph/0112367v1>

This figure "fig2.jpg" is available in "jpg" format from:

<http://arXiv.org/ps/astro-ph/0112367v1>







This figure "fig4.jpg" is available in "jpg" format from:

<http://arXiv.org/ps/astro-ph/0112367v1>

This figure "fig5.jpg" is available in "jpg" format from:

<http://arXiv.org/ps/astro-ph/0112367v1>

